Decoupling high surface recombination velocity and epitaxial growth for silicon passivation layers on crystalline silicon

Landheer, Kees; Kaiser, Monja; Verheijen, Marcel A.; Tichelaar, Frans D.; Poulios, Ioannis; Schropp, Ruud E I; Rath, Jatin K.

Important note
To cite this publication, please use the final published version (if applicable).
Please check the document version above.

Decoupling high surface recombination velocity and epitaxial growth for silicon passivation layers on crystalline silicon

Kees Landheer[1], Monja Kaiser[3], Marcel A Verheijen[2], Frans D Tichelaar[4], Ioannis Poulios[1], Ruud E I Schropp[1] and Jatin K Rath[1]

[1] Faculty of Science, Debye Institute for Nanomaterials Science-Physics of Devices, Utrecht University, High Tech Campus 21, 5656 AE Eindhoven, The Netherlands
[2] Department of Applied Physics, Plasma & Materials Processing, Eindhoven University of Technology, PO Box 513, 5600 MB Eindhoven, The Netherlands
[3] Philips Innovation Services, High Tech Campus 11, 5656 AE Eindhoven, The Netherlands
[4] National Centre for HREM, Kavli Institute of Nanoscience Delft, Delft University of Technology, Lorentzweg 1, 2628 CJ, Delft The Netherlands

E-mail: c.landheer@uu.nl

Abstract

We have critically evaluated the deposition parameter space of very high frequency plasma-enhanced chemical vapour deposition discharges near the amorphous to crystalline transition for intrinsic a-Si:H passivation layers on Si (1 1 1) wafers. Using a low silane concentration in the SiH_4–H_2 feedstock gas mixture that created amorphous material just before the transition, we have obtained samples with excellent surface passivation. Also, an a-Si:H matrix was grown with embedded local epitaxial growth of crystalline cones on a Si (1 1 1) substrate, as was revealed with a combined scanning electron and high-resolution transmission electron microscopy study. This local epitaxial growth was introduced by a decrease of the silane concentration in the feedstock gas or an increase in discharge power at low silane concentration. Together with the samples on Si (1 1 1) substrates, layers were co-deposited on Si (1 0 0) substrates. This resulted in void-rich, mono-crystalline epitaxial layers on Si (1 0 0). The epitaxial growth on Si (1 0 0) was compared to the local epitaxial growth on Si (1 1 1). The sparse surface coverage of cones seeded on the Si (1 1 1) substrate is most probably enabled by a combination of nucleation at steps and kinks in the {1 1 1} surface and intense ion bombardment at low silane concentration. The effective carrier lifetime of this sample is low and does not increase upon post-deposition annealing. Thus, sparse local epitaxial growth on Si (1 1 1) is enough to obstruct crystalline silicon surface passivation by amorphous silicon.

Keywords: SHJ solar cell, epitaxial growth, cc VHF PECVD, surface passivation

[S] Supplementary material for this article is available online

(Some figures may appear in colour only in the online journal)

1. Introduction

The use of intrinsic amorphous silicon (i-a-Si:H) buffer layers that passivate the wafer surface in the silicon heterojunction (SHJ) solar cell is a proven concept and results in crystalline silicon-based solar cells with world record energy efficiencies. In 2015, an energy efficiency of 25.1% with an open circuit voltage (V_{oc}) of 738 mV was reported for a bifacial SHJ solar cell [1].

A critical step in the processing of SHJ solar cells is the formation of the c-Si/i-a-Si:H interface. A poor interface has a high density of Si dangling bond defects near the middle of the

band gap that facilitates Shockley–Read–Hall recombination. A good *c*-Si/a-Si:H interface in a SHJ solar cell is an abrupt transition from mono-crystalline to amorphous material with a silicon dangling bond density (D_{it}) below 10^{10} cm^{-2} eV^{-1} (corresponding to 1 dangling bond per 10^5 Si surface atoms) [2, 3]. If D_{it} is above 10^{10} cm^{-2} eV^{-1}, it can be reduced by the formation of Si–Si or Si–H covalent bonds, for example in a post-deposition anneal process. This is called chemical passivation of defects. Another way to avoid recombination at the interface is field-effect passivation, but this passivation mechanism alone cannot warrant high-performance solar cell operation at high injection level ($>10^{15}$ cm^{-3}), i.e. under peak daylight conditions [4]. Therefore, we focus in this paper on the plasma-enhanced chemical vapour deposition (PECVD) processing of a-Si:H layers with the objective to precisely define the regime for optimal chemical surface passivation, which is quantified by the effective minority carrier lifetime (τ_{eff}).

Two post-deposition treatments have been reported to reduce D_{it}: annealing (preferably in a H$_2$ containing atmosphere) [5] and H$_2$ plasma treatment [6–8]. The annealing process enables atomic hydrogen (H) diffusion through the a-Si:H network. The best a-Si:H passivation samples are produced by low-temperature deposition at 130 °C and subsequent post-deposition annealing [9] and this method is the object of this study. Street *et al* [10] report that a deposition temperature of 130 °C is the equilibration temperature for bonded hydrogen in amorphous silicon and, therefore, the hydrogen content of PECV layers deposited at 130 °C is relatively high [11]. The passivation samples deposited with $T_{subs} = 130$ °C are known to result in excellent passivation layers after annealing [9, 12]. The best a-Si:H passivation layers are grown with deposition conditions near the amorphous to epitaxial growth transition [13]. It is generally accepted that epitaxial Si growth should be avoided, since this usually creates a rough c-Si/a-Si:H interface with a high density of recombination centres [3, 5]. A relevant question is how many atomic layers at the c-Si/a-Si interface contribute to the interface defect density D_{it}. De Wolf *et al* [14] wrote that this is determined by the electron wavefunction penetration depth into the a-Si. They indicated that a penetration depth of 10 nm is a realistic estimate. The i-a-Si:H buffer layer of a SHJ solar cell is only 4 nm thick [15], and, therefore, the complete i-a-Si:H layer is involved in the D_{it}.

Technically, the silane fraction in the SiH$_4$–H$_2$ gas feedstock ($S_F(\%) = [\text{SiH}_4]/[\text{H}_2] \times 100$)) of the PECVD discharge has repercussions on the as-deposited quality of the a-Si:H passivation layers and on the effectiveness of the post-deposition annealing. If a large silane fraction is used, the short deposition time does not allow correction for small initial fluctuations in the plasma parameters. Therefore, a small silane fraction with low deposition rate is preferred as this gives better control over the plasma conditions and results in a more homogeneous and reproducible layer. We investigate in this study the growth of a-Si:H at low S_F, low pressure, and low substrate temperature conditions.

The presence and nature of epitaxy strongly depends on the substrate orientation. For example, a perfectly monocrystalline epitaxial Si layer is grown on the Si (1 0 0) facet while a complete amorphous Si layer is grown on Si (1 1 1) facets within the same deposition run [16, 17]. The highest efficiency for SHJ solar cells is obtained with a pyramidal surface texture of a Si (1 0 0) wafer. The facets of these pyramids are Si {1 1 1} crystal planes. Since results for i-a-Si:H passivation samples obtained on Si(1 0 0) are not directly applicable to the Si (1 1 1) surface, a-Si:H growth is best studied on polished Si (1 1 1) wafers. The texturization process usually creates pyramids with some crystal defects, especially in the valleys between the pyramids [18]. These defects expose among other Si {1 0 0} surfaces. Therefore, we also investigate in this study the Si growth on Si (1 0 0) wafers for deposition conditions resulting in the best passivation layers on Si (1 1 1).

The condition of the c-Si surface prior to Si growth also has a crucial influence: a chemical or thermal oxide of only 2 nm can prevent epitaxial growth [19, 20]. In this study, we briefly dip the wafer in hydrofluoric acid (HF) solution, prior to a-Si:H deposition on the wafer. Hricovini *et al* [21] showed that an HF dip of a Si (1 1 1) wafer creates an unreconstructed (1 1 1) surface with Si–H termination, which is not affected by annealing. However, the Si–H termination on the flat wafer can be lost as a consequence of the PECVD process and in this study we observed that sparse conical crystalline growth seeded at this surface is possible.

2. Experimental

The c-Si/a-Si:H interface in this study is formed in three processing steps: dipping a Si wafer in dilute HF (1%) solution for 120 s (unless otherwise noted), deposition of the a-Si:H with 60 MHz VHF (very high frequency) PECVD at a substrate temperature $T_{subs} = 130$ °C, and annealing for 210 min at 230 °C in an oven with nitrogen gas. To evaluate the chemical passivation quality, we deposited i-a-Si:H layers on both sides of a double-sided polished float zone (FZ) Si (1 1 1) wafer. The *n*-type FZ wafer is 280 ± 25 μm thick, has a resistivity of 3.5 ± 1.5 Ω cm (doping level 1–4×10^{15} cm^{-3}) and is delivered by the supplier vacuum-sealed with a 2 nm thick RCA oxide on the surface. Simultaneously with the depositions on Si (1 1 1) wafer, Si layers were co-deposited on HF-cleaned Si (1 0 0) substrates. The PECVD reactor for the silicon depositions is described in figure 1 and elsewhere [22]. A series of passivation samples with silane fractions $S_F = 1.7$–9.1 % (total flow 60 sccm, pressure 25 Pa) was deposited with growth rates varying from 0.14 nm s^{-1} up to 0.5 nm s^{-1} [23] at a discharge power of $P_{rf} = 40$ mW cm^{-2}. Subsequently, the parameter space near the amorphous to epitaxial growth transition was further explored by increasing the discharge power from 40 to 57 mW cm^{-2} in the S_F series.

Effective lifetimes (τ_{eff}) of the passivation samples were measured with a Sinton WCT-120: the quasi steady-state photoconductance method was used for lifetimes below 100 μs and the transient photoconductance decay (TPCD) method was used for lifetimes above 100 μs [24]. τ_{eff} as a function of minority carrier injection level (Δn) can be split in a recombination lifetime in the bulk $\tau_b(\Delta n)$ and on the surface $\tau_s(\Delta n)$ and is computed as follows [9]:

J. Phys. D: Appl. Phys. **50** (2017) 065305

K Landheer *et al*
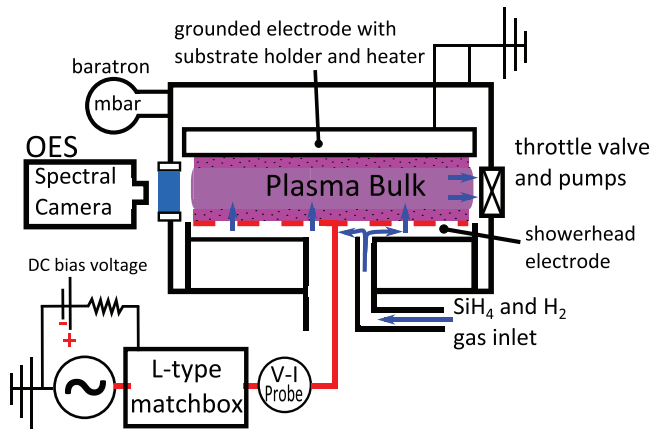
Figure 1. Diagram of the parallel plate reactor used for VHF PECVD of the intrinsic a-Si:H layers in this study and plasma diagnostics. An externally applied bias voltage ($V_{ext, DC}$) can be superimposed on the DC bias (V_{DC}) at the powered electrode with the DC bias voltage circuit.

$$\frac{1}{\tau_{eff}(\Delta n)} = \frac{1}{\tau_b(\Delta n)} + \frac{1}{\tau_s(\Delta n)} = \frac{1}{\tau_b(\Delta n)} + \frac{2S_{eff}(\Delta n)}{W} \quad (1)$$

where W is the thickness of the wafer (280 μm) and S_{eff} the effective surface recombination velocity. For the FZ wafers that we used, the minority carrier diffusion length is much longer than the wafer thickness and, therefore, τ_b is much larger (>20 ms below $\Delta n = 1 \times 10^{15}$ cm^{-3}) than τ_s and thus the $1/\tau_b$ term is neglected when surface passivation is studied. Here, we report τ_{eff} at the minority carrier injection level $\Delta n = 1 \times 10^{15}$ cm^{-3} unless otherwise noted. The implied open-circuit voltage ($V_{oc, imp}$) can be determined from the quasi-Fermi level splitting at 1 sun (AM1.5 spectrum with an intensity of 100 mW cm^{-2}) [24]. The light intensity, measured by a reference photodiode, and the injection level, are measured simultaneously by the Sinton setup.

$$V_{oc,imp} = \frac{k_B T}{q} \ln\left[\frac{(N_x + \Delta n)\Delta n}{n_i^2} + 1\right] \quad (2)$$

where $k_B T/q$ is the thermal voltage at room temperature (25 mV), N_x is the doping level of the wafer, n_i the intrinsic carrier concentration at room temperature ($n_i = 8.6 \times 10^9$ cm^{-3}), and Δn the injection level at 1 sun. For our passivation samples, Δn at 1 sun varied between 1.3×10^{15} and 1.3×10^{16} cm^{-3}.

With high-resolution transmission electron microscope (HR-TEM) images we investigated the structural properties of the c-Si/a-Si:H interface in real space and in reciprocal space (fast Fourier transform (FFT)), by diffraction and with high-angle annular dark field (HAADF) scanning transmission electron microscopy (STEM) imaging. To obtain electron transparent samples, focused ion beam (FIB) preparation is used. Both carbon and platinum layers are used as protection and deposited before FIB preparation (figure 2). HR-TEM studies are performed with a JEOL ARM200F operated at 200 kV. For the HR-TEM image of figure 9 a Tecnai TF20ST (200 kV) was used. In this case, the cross-section of the
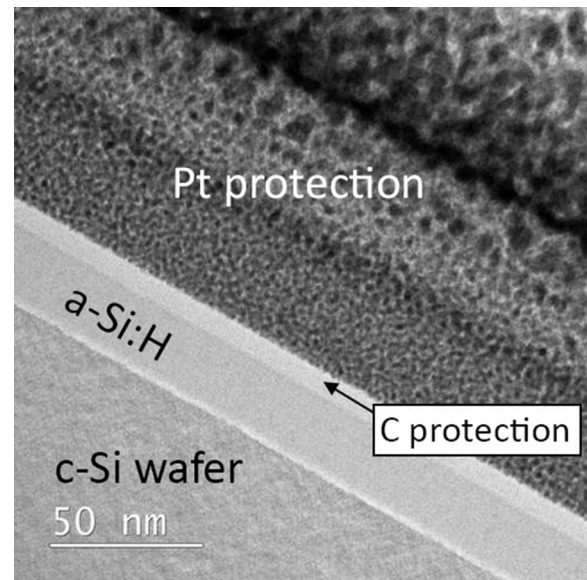
Figure 2. A cross-section TEM image showing the carbon (C) and platinum (Pt) protection layers that were deposited on the passivation sample prior to FIB preparation of the c-Si/a-Si:H interface with HR-TEM.
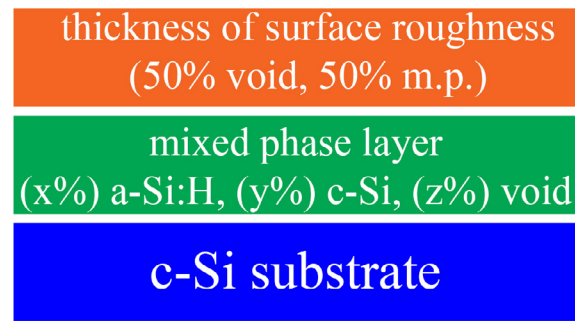
Figure 3. Schematic diagram showing a cross-section of the layer stack used for SE modelling: on top of the c-Si substrate a single or mixed phase layer and a surface roughness layer was modelled with the BEMA ($x\% + y\% + z\% = 100\%$).

sample was prepared by conventional mechanical polishing and Ar ion milling, while protecting the surface with glass glued on top.

The thickness of the deposited Si layers was determined by HR-TEM and/or by spectroscopic ellipsometry (SE) measurements with a Woollam VASE system. Mixed phase Si layers can be modelled with a Bruggeman effective-medium approximation (BEMA). With the BEMA, the amorphous, polycrystalline (poly-Si), and void fraction in the mixed phase layer can be fitted (see figure 3). The thickness of the surface roughness is also determined with the BEMA with a surface layer consisting of 50% void and 50% of the mixed phase (m.p.) layer material.

Amorphous Si is direct band-gap semiconductor material and its photon absorption in the spectral range from 1.5–5.0 eV can be modelled with a Tauc–Lorentz (TL) harmonic oscillator. The parametrization of Jellison and Modine [25] is used here to fit the pseudo-electric function ε_2:

J. Phys. D: Appl. Phys. **50** (2017) 065305

K Landheer *et al*

$$\eta_2(E > E_g) = \frac{A\, E_0 Br(E - E_g)^2}{(E^2 - E_0{}^2)^2 + Br^2 E^2} \cdot \frac{1}{E} \qquad (3)$$

where A is the denseness parameter and Br is the film disorder parameter. E_0 is the peak position of the TL-harmonic oscillator and E_g is the Tauc band-gap energy. E_g can be found by fitting both pseudo-electric functions ε_1 and ε_2 to the SE data.

With Fourier transform infrared spectroscopy (FTIR) with a Bruker Vertex 70, we measured the light absorbance of the a-Si:H layers in the spectral range 380–3500 cm^{-1} in a transmission setup. The atomic density of hydrogen bonded to Si atoms (c_H) and the microstructure parameter R^* of the a-Si:H material were determined with this absorption spectrum. c_H in the a-Si:H network is determined from the absorption peak at 640 cm^{-1} using the method of Langford *et al* [11]. We used $c_H = 100 * n_H/(n_H + n_{Si})$, with the silicon atomic density being $n_{Si} = 5 \times 10^{22}$ cm^{-3}. The microstructure parameter R^* is the percentage of high stretching mode (HSM) at 2080 cm^{-1} in a mixture with the low stretching mode at 2000 cm^{-1}, i.e. $R^* = I_{2080}/(I_{2000} + I_{2080})$. The Si–H$_2$ complex also has a bending mode [11, 26] around 880 cm^{-1} and this helps us to determine the contribution of Si–H$_2$ to the HSM peak. The integrated absorbance ratio of the Si–H$_2$ bending mode to the HSM is $R^B = I_{880}/I_{2080}$. For the epitaxial layers on Si(1 0 0) we used the ratio: $R^{*\prime} = I_{2114}/(I_{2000} + I_{2114})$. Interference fringes from reflections at the polished surface are negligible, since the wafer is measured at a 10° angle from perpendicular incidence. A B-spline polynomial is used for the background subtraction.

3. Results

This results section is structured as follows. First, the effective lifetime upon annealing of symmetric passivation samples created with the silane fraction (S_F) series at $P_{rf} = 40$ mW cm^{-2} is shown. This is shown for 24 and 44 nm thick a-Si:H layers. Also, the effective lifetimes of two selected samples deposited with $S_F = 1.7$ and 5.3% (with layer thickness of 86 and 67 nm, respectively) at $P_{rf} = 57$ mW cm^{-2} are given. The structural properties of this set of samples are then discussed. Finally, the sample with sparse local epitaxial growth on Si (1 1 1) is discussed in detail, complemented by a study of the epitaxial growth of the co-deposition on Si (1 0 0).

3.1. Passivation quality properties of a-Si:H layers

We observed in the S_F series of the annealed passivation samples (see figure 4), that the highest effective lifetime was achieved at the lowest S_F. The highest τ_{eff} of 11.6 ms ($V_{oc, impl} = 729$ mV) was achieved for 44 nm thick a-Si:H layers deposited at $S_F = 1.7$% (sample I in table 1). In a flat SHJ cell we made a 3 ± 1 nm thick i-a-Si:H buffer layer with our best passivating a-Si:H material and achieved an energy conversion efficiency of 17.2% ($V_{oc} = 0.65$ V, FF = 71%, $J_{sc} = 36.9$ mA cm^{-2}) under 100 mW cm^{-2} light with AM1.5 spectrum. The n- and p-layer and contact layers of the SHJ cell were made with recipes previously applied in our research group
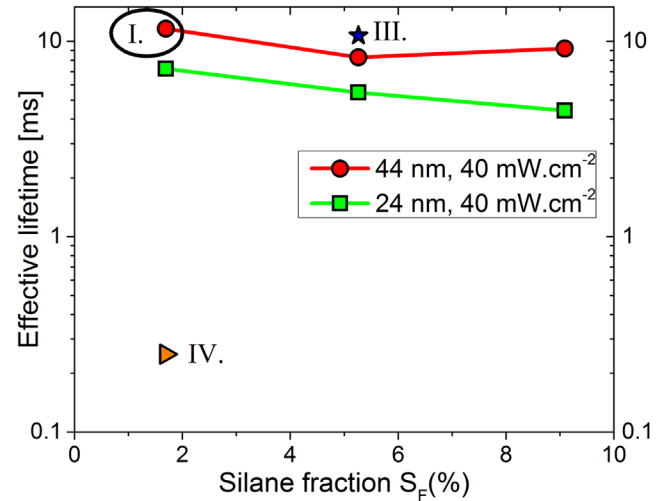
Figure 4. Effective lifetimes of passivation samples after post-deposition annealing. The extra data points III and IV label conditions in the a-Si:H to c-Si:H transition regime and their deposition conditions are given in table 1.

[12]. A passivation sample with identical i-a-Si:H layers, only 24 nm thick instead of 44 nm, resulted in a slightly lower lifetime after annealing ($\tau_{eff} = 7.2$ ms). The vertical order of the data points at $S_F = 5.3$% in figure 4 can be the result of differences in layer thickness: sample III has a thickness of 67 nm (see table 1). Leendertz *et al* [4] also observed with TPCD measurements and simulations that the effective lifetime is less with thinner intrinsic layers. This indicates that defects at the a-Si:H surface can limit the lifetime measured with the TPCD method.

The results presented in figure 4 and table 1 also show that the passivation quality of the layers is sensitive to even small changes in the plasma conditions at $S_F = 1.7$%, especially near the amorphous to epitaxial growth transition. An increase in P_{rf} from 40 to 57 mW cm^{-2} at $S_F = 1.7$% reduced the annealed lifetime from 11.6 to 0.25 ms. A decrease in silane fraction from 5.3% to 1.7% at $P_{rf} = 57$ mW cm^{-2} (samples III and IV) resulted in a similar lifetime reduction. Sample IV was the only sample in figure 4 with an as-deposited τ_{eff} above 0.1 ms, namely $\tau_{eff} = 0.24$ ms, and this lifetime did not change upon annealing.

3.2. Structural properties of the Si layers close to the transition

The structural properties of the samples labelled I–V, deposited near or in the a-Si:H to crystalline transition regime, are studied with FTIR, SE and a representative set of these samples also with HR-TEM (last column of table 1). Deposition conditions, effective lifetimes both in the as-deposited and the annealed state, and material properties are given in table 1. The microstructure values R^* of the samples deposited at $S_F = 1.7$% are higher than at $S_F = 5.3$%, but no correlation between R^* and S_F can be observed in figure 5. The HSM at 2080 cm^{-1} can be attributed to monohydrides (Si–H) on the surface of nanovoids or multihydrides (Si–H$_x$ with $x > 1$). The integrated absorbance ratio of the Si–H$_2$ bending mode to

J. Phys. D: Appl. Phys. **50** (2017) 065305

K Landheer *et al*

Table 1. Deposition parameters, effective lifetimes in the as-deposited and in the annealed state, and properties of the Si layers deposited at $T_{sub} = 130\,°C$.

No.	facet	P_{rf} (mW cm^{-2})	S_F (%)	τ_{eff}, as dep. (ms)	τ_{eff}, as ann. (ms)	R^*	c_H (%)	th.[a] (nm)	TEM (y/n)
I[b,c]	(1 1 1)	40	1.7	<0.10	11.6	0.43	17.7	44	y
II	(1 0 0)	40	1.7	n/a[d]	n/a[d]	0.80[e]	4.4	52	n
III	(1 1 1)	57	5.3	0.07	10.7	0.30	17.8	67	n
IV[c]	(1 1 1)	57	1.7	0.24	0.25	0.48	17.9	86	y
V[d]	(1 0 0)	57	1.7	n/a[d]	n/a[d]	0.75[e]	5.8	95	y

[a] Layer thicknesses are based on SE modelling and HR-TEM images, if available.
[b] This recipe was used for the i-a-Si:H buffer layer in a flat SHJ solar cell.
[c] Sample sets I and II and set IV and V were co-deposited.
[d] Samples II and V are not passivation samples (n/a means not applicable).
[e] The microstructure of samples II and V is defined as $R^{*'} = I_{2114}/(I_{2114} + I_{2000})$.

the HSM of sample IV is $R^B = I_{880}/I_{2080} = 0.38$, which is not much different from the ratios of samples I and III: for sample I $R^B = 0.42$, and for sample III $R^B = 0.41$. Thus, the Si–H$_2$ bending mode is present in all passivation samples (i.e. I–IV).

In figure 6(a) (samples I, III, and IV) and (b) (samples II and V) the SE modelling results are shown. The peak position of the pseudo-dielectric function ε_2 that models a-Si:H is at 3.7 eV for samples I and III and this infers that they consist of purely amorphous silicon. The hydrogen content of these a-Si:H samples varied between 17.7% and 17.9%, which agrees well with values found in the literature for passivation samples deposited at low substrate temperatures [11, 27]. For sample IV, on the other hand, the T–L oscillator peak is shifted towards the c-Si peak at 4.2 eV and this indicates the presence of crystalline inclusions. Moreover, the peak is slimmer, which is reflected in the small value for the disorder parameter Br. For the fit of sample IV presented in figure 6(a), the measured SE data was modelled with purely amorphous silicon instead of a mixed phase layer. If a fit is performed with a small poly-crystalline Si (%) fraction (e.g. 7%) in the mixed phase layer, the mean squared error did not change significantly. The surface roughness layer thickness was 8 nm thick, whereas for the other samples the roughness was below 1.5 nm. The inset table of figure 6(a) shows that the a-Si:H deposited at $P_{rf} = 40$ mW.cm^{-2} (sample I) has a higher denseness parameter A than the a-Si:H deposited at $P_{rf} = 57$ mW cm^{-2} (samples III and IV). The disorder parameter Br of the a-Si:H is about 2.15 eV for samples I and III. The A and Br of sample I are similar to the values reported by Rath *et al* [28] for device quality a-Si:H deposited with VHF PECVD at 100 °C with $S_F = 5\%$.

Samples II and V are epitaxial Si layers on HF-cleaned Si (1 0 0). The thickness of the epitaxial layer of sample V has been determined by cross-section HR-TEM. This thickness was subsequently used as input for the SE modelling (see figure 6(b)). With a BEMA model consisting of a mixture of polycrystalline Si and voids, we determined the void fraction to be 5.5% of the volume. This is a large void fraction, which could have been created by chemical sputtering of Si by H_y^+ ions. Chemical sputtering was previously observed under the aggressive plasma deposition conditions used to deposit this sample [22]. The chemical sputtering rate, which is among others proportional to the H_y^+ flux, can be reduced by reducing
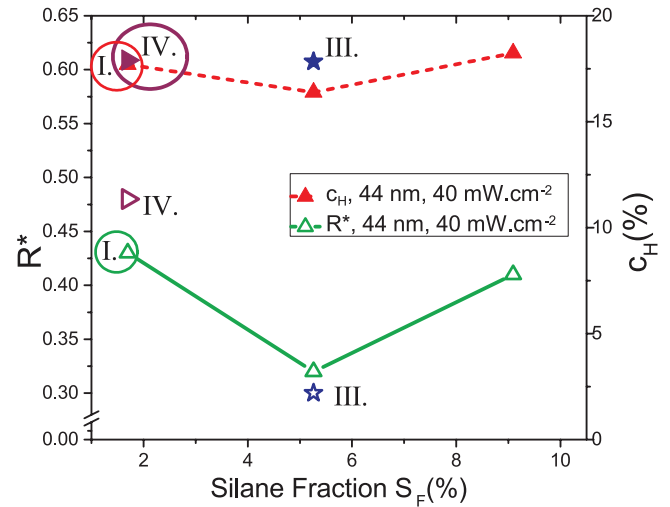
Figure 5. The microstructure factor R^* (open symbols) and the bonded hydrogen content c_H (closed symbols) were determined with the FTIR spectra of the passivation samples depicted in figure 4.

the P_{rf} to 40 mW cm^{-2}. Sample II was deposited at $P_{rf} = 40$ mW cm^{-2} and its void fraction was indeed lower with 3.5% of the volume. The reduction in void fraction can be observed in figure 6(b): the pseudo-dielectric function ε_2 of sample II is closer to the c-Si substrate function than the function of sample V.

In the FTIR spectrum of sample V displayed in figure 7, we discern two Si–H$_2$ bending modes at 848 and 894 cm^{-1} and three SiH$_x$ stretching modes at 1905, 2000, and 2114 cm^{-1}. The peak at 2114 cm^{-1} is attributed to SiH$_2$ bonded on the wafer or void surface [29]. The peak at 2000 cm^{-1} is attributed to Si–H bonds in the epitaxial layer and the peak at 1905 cm^{-1} is attributed to Si–H bonds with a Si dangling bond as its first neighbour [30]. The peak at 1905 cm^{-1} was not observed in the FTIR spectrum of sample II. These IR peaks confirm the crystalline nature of the layer. We determined the hydrogen content of sample V to be $c_H = 5.8\%$, based on the peak at 640 cm^{-1} using the same proportionality constant as used for amorphous silicon [11]. Microcrystalline Si growth with similar hydrogen content has been reported in the literature for layers close to the transition regime [31].

J. Phys. D: Appl. Phys. **50** (2017) 065305

K Landheer *et al*
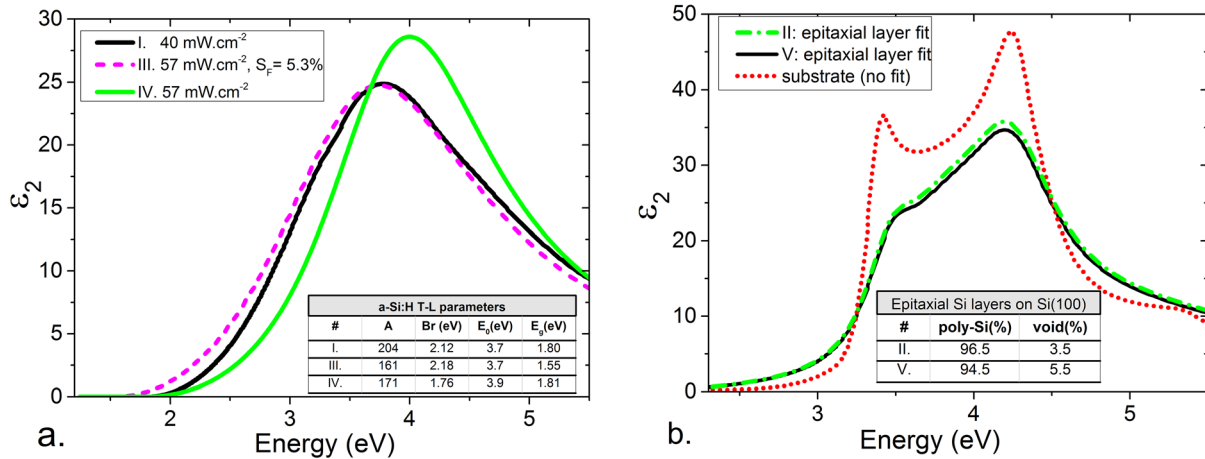
Figure 6. Fits of the pseudo-dielectric function ε_2 (eV) for (a) the a-Si:H *T–L* oscillator of samples I, III, and IV and (b) the mixed phase (poly-Si(%) plus void(%)) epitaxial layer of samples II and V and the pseudo-dielectric function ε_2 of the Si substrate.

3.3. HR-TEM: the substrate/layer interface of samples I, IV, and V

In figure 8, the c-Si/a-S:H interface of sample I is displayed. This sample has an effective lifetime of 7.2 ms upon annealing. The image shows a purely amorphous layer and this confirms the SE modelling results. At the c-Si/a-Si:H interface, a sharp change in darkness is observed, that contains no discernable low-density interface layer that would be indicative of an interface oxide. In figure 9, we show an HR-TEM image of the c-Si surface after a 3 min HF dip and regrown native oxide in ambient atmosphere on a Si (1 1 1) wafer: a few monolayers of roughness from kinks, steps, and ad-atoms remain on the wafer surface.

Sample IV, deposited at a slightly higher power density than sample I, consists predominantly of a-Si:H (see figure 10). The c-Si/a-Si:H interface of this sample, displayed in figure 8, is sparsely interrupted with the seeded growth of crystalline cones. The surface coverage of the crystalline cones, determined with a top view scanning electron microscope (SEM) image (see figure 11), is only 21 cones per μm^2. Two cones are displayed in the HR-TEM images of figures 10(a)–(f), both starting at the substrate surface and having an epitaxial relation to it. It is most likely that all cones in sample IV are seeded at the substrate, since no cones starting away from the substrate surface were found. Moreover, a sample that was grown under identical conditions on a Si (1 0 0) wafer with a 2 nm RCA oxide layer (not HF-dipped) showed neither crystallinity in SE modelling nor cones protruding from the sample surface in top-view SEM. Apart from the cone structures, no crystallinity is visible in the a-Si:H matrix of figures 10(a),(b) and (d) as also evidenced from the FFT of the amorphous matrix (see inset of figure 10(c)).

In figure 10(c), we take a closer look at the origin of the cones and observe changes in crystal growth direction in the first 20 nm of the cone as a result of two twin operations along two different rotation axes (see supplementary material (stacks.iop.org/JPhysD/50/065305/mmedia)). The first horizontal epitaxial crystal planes have a very small angle of about 1.5° with the plane parallel to the substrate surface,
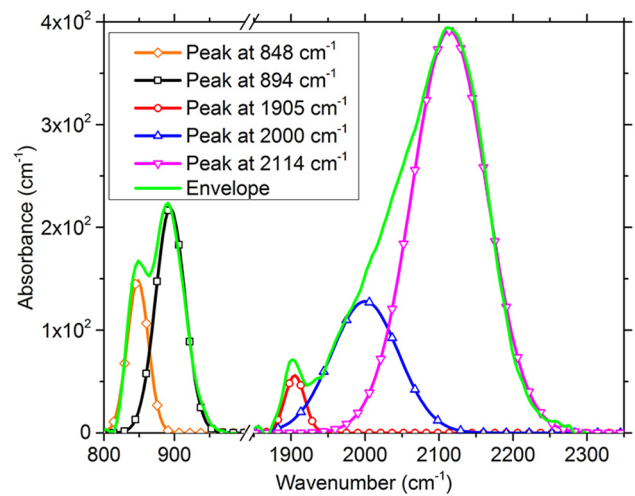
Figure 7. The FTIR spectrum of sample V. The green envelope of the bending modes is composed of Gaussian peaks at 848 and 894 cm^{-1}. The green envelope of the stretching modes is composed of Gaussian peaks at 1905, 2000, and 2114 cm^{-1}.

implying some degree of freedom w.r.t. perfect epitaxy due to the limited lateral size of the origin of the cone. The arrow in figure 10(c) indicates a twin boundary. In figure 10(f), the cone starts with growth in the ⟨1 1 1⟩ direction, exhibiting a high density of twin boundaries perpendicular to the growth direction. The zigzag-like morphology of this part of the cone indicates the tendency of the crystal to form {1 1 1} side facets, making an angle of 71° with the substrate surface. At a height of roughly 18 nm the cone widens as a result of a more complex defect geometry. At this height, two non-identical stacking faults occur: the right side of the crystalline cone continues the ⟨1 1 1⟩ growth direction, still exhibiting twin planes orthogonal to the growth direction (see also figure 10(b)). In contrast, the left side changes growth direction, most likely due to {1 1 1} twin planes with directions inclined to the growth direction. The spotty contrast in this region reflects differences in diffraction contrast for the different crystalline orientations resulting from multiple twinning events. From bottom to top, the cones have a height of about 95 nm, similar
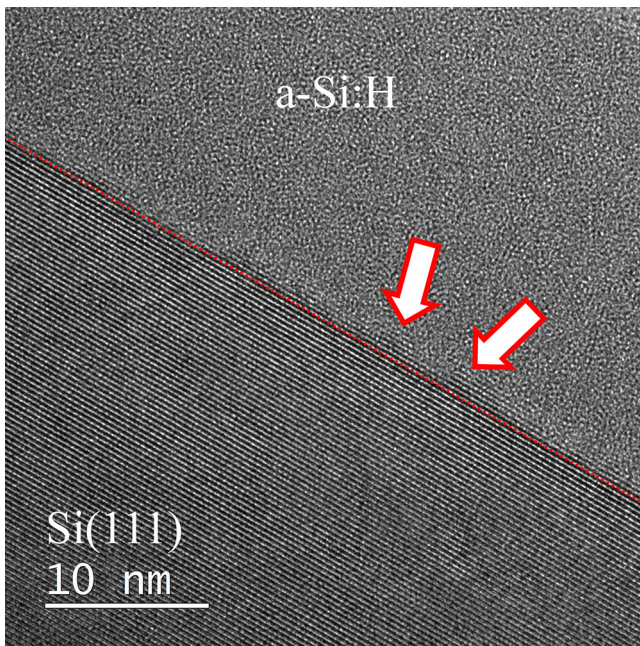
Figure 8. HR-TEM micrograph obtained along the ⟨1 1 2⟩ zone axis showing the c-Si (1 1 1)/a-Si:H interface of the annealed passivation sample I with some surface roughness indicated by the arrows. The red dotted line indicates the boundary between the wafer substrate and the deposited Si layer.
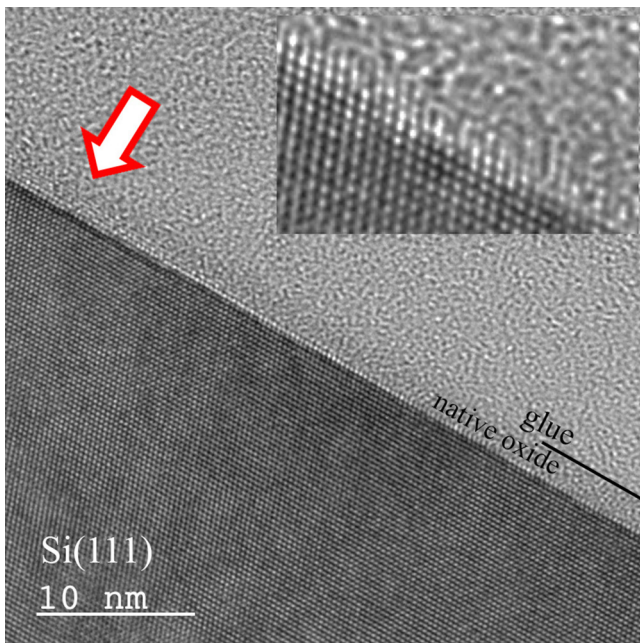
Figure 9. HR-TEM image obtained along the ⟨1 1 0⟩ zone axis after 3 min HF dip and regrown native oxide in ambient atmosphere on a Si (1 1 1) wafer. The arrow shows an area with surface roughness, also visible in another area in the inset.

to the epitaxial layer thickness of sample V. The amorphous matrix, however, is only 86 nm thick (given in table 1) and this thickness is used as the input parameter for the SE modelling of this sample. The etching rate of Si during PECVD by a SiH₄–H₂ discharge [32] or when a pure H₂ plasma is applied depends on the crystallinity of the material: a-Si:H is etched at

a higher rate than (μ)c–Si [33]. Therefore, the a-Si:H matrix is thinner than the protruding crystalline cones.

Sample II and V are epitaxial layers deposited on Si (1 0 0) substrates. Sample IV (figure 12) and V (figure 12) were deposited in the same deposition run on Si (1 1 1) and Si (1 0 0), respectively. The HR-TEM images of sample V in figure 12 are used to help to explain the local epitaxial growth on Si (1 1 1). The HR-TEM image of figure 12(a) displays a spotty contrast. The FFT pattern of the selected area in figure 12(a) is a single crystalline pattern, without any evidence of additional spots due to twin domains. Thus, this layer must be considered as being monocrystalline. The origin of the spotty contrast is visible in figures 12(b) and (c): the film contains a high density of voids. The spotty contrast most likely is the result of differences in projected density as well as local lattice distortions around the voids. The top surface of the epitaxial layer is relatively flat with only a few monolayers of roughness (figure 12(e)). The thickness of the roughness layer modelled with SE is below 1.5 nm for sample II and V.

4. Discussion

Passivation sample I had a sharp c-Si/a-Si:H interface and showed excellent surface passivation with a τ_{eff} of 7.2 ms after annealing. Excellent surface passivation is expected for i-a-Si:H that is deposited with deposition conditions close to the amorphous to crystalline Si transition [13]. For sample I, we used the deposition parameters $S_{\mathrm{F}} = 1.7\%$ and $P_{\mathrm{rf}} = 40$ mW cm^{-2}. By increasing P_{rf} to 57 mW cm^{-2}, we observed an as-deposited $\tau_{\mathrm{eff}} = 0.24$ ms for sample IV that does not increase with post-deposition annealing. Already sparse local epitaxial growth in the a-Si:H matrix deteriorated the surface passivation quality obtained after annealing. Our best passivation samples (I and III), on the other hand, had an abundance of defects after deposition, which resulted in an as-deposited effective lifetime below 100 μs. The defects were mostly Si dangling bonds at or near the c-Si/a-Si:H interface and were readily passivated by post-annealing at temperatures above 180 °C [9] due to the enhanced mobility of atomic H. The atomic H reduced the number of defects at the interface by forming covalent Si–H bonds with Si dangling bonds and most probably induced some network reconstruction [14, 27].

In contrast to our results, Descoeudres *et al* [13] observed that by increasing the dissipated power in the VHF PECVD discharge the effective lifetime upon annealing of a-Si:H passivation samples was improved. However, those layers were deposited from pure silane feedstock gas. Fujiwara *et al* [3] showed that for substrate temperatures above 140 °C, epitaxial growth on Si (1 0 0) can be prevented by increasing the discharge power. They found that both a rise in discharge power and a higher resistivity of the wafer substrate increases the ion bombardment energy. They concluded that the higher ion bombardment energy prevented epitaxial growth. In our S_{F} series, the peak ion energy in the ion energy distribution function stayed almost constant with increasing S_{F}: at $P_{\mathrm{rf}} = 40$ mW cm^{-2} the peak SiH₃⁺ ion energy was at 24 eV and at $P_{\mathrm{rf}} = 57$ mW cm^{-2}

J. Phys. D: Appl. Phys. 50 (2017) 065305

K Landheer *et al*
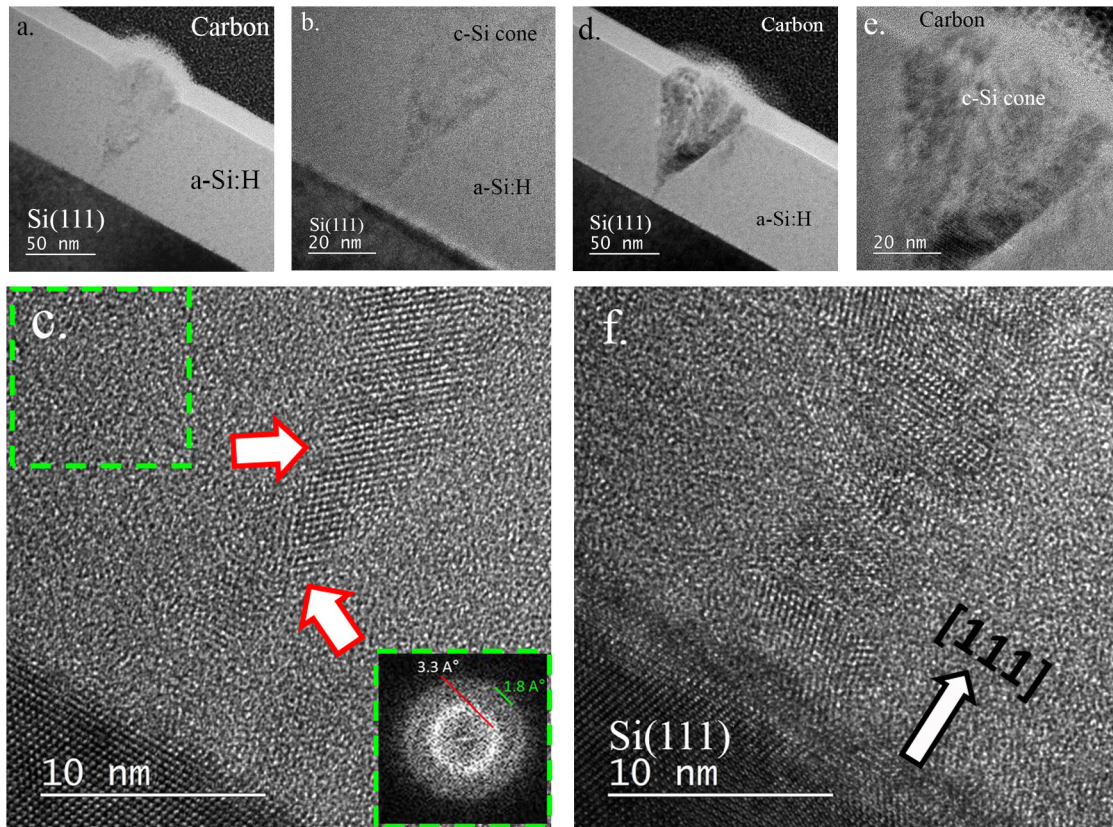
Figure 10. Sample IV: (a) and (b). Seeded crystalline growth inside an amorphous Si network. (c) The arrow indicates a change in crystal growth direction, i.e. twin boundaries. The FFT in the lower right corner is taken in the amorphous region within the green dashed square. The FFT is identical to the FFT of a perfectly amorphous Si network: no crystalline features can be discerned. (d) Crystalline growth from the substrate to the top of the layer. (e) The crystalline cone has regions with different contrast, which are separated by twin boundaries. The difference in contrast is a result of the different stacking orientation. (f) A zoom-in on the interface of the wafer at the origin of the cone displaying epitaxial growth with twin boundaries orthogonal to the growth direction. The c-Si surface has a roughness of 1–2 monolayers. All images were acquired along the $\langle 1\,1\,0 \rangle$ zone axis of the substrate.

the peak ion energy was at 29 eV [22]. Thus, the peak ion energies were above the threshold ion energy for surface atom displacement (16 eV), but below the threshold for energy for bulk Si atom displacement (36 eV) [34]. However, we saw local epitaxial growth in an amorphous Si network on the Si (1 1 1) substrate during deposition with low silane concentration and at low substrate temperature. The sparse and continuous conical growth is not likely to be related to a chemical effect such as atomic hydrogen-induced crystallization [35] or H_y^+ chemical sputtering [22]. Probably, there is a window of ion bombardment intensity (a combination of ion flux and energy) that results in a more equilibrated Si growth. This is possible when the energy supplied by the ions enhances the diffusion of growth precursors on the cold surface. In our study on the $Si_xH_y^+$ flux trend in the S_F series at $P_{rf} = 57$ mW cm^{-2}, we observed that the $Si_xH_y^+$ ion bombardment at low silane concentration is intense [22]. 30% of the Si atoms deposited at $S_F = 1.7\%$ are from $Si_xH_y^+$ ions, and the remainder of the silicon deposited is from dissociation products such as the SiH_3 radical. At $S_F = 20\%$ the ion contribution to the silicon growth rate is only 10%. Similar results were also observed by Hamers *et al* [36]. Apart from the seeded crystalline cones, no crystalline inclusions were found in the amorphous matrix of sample IV.
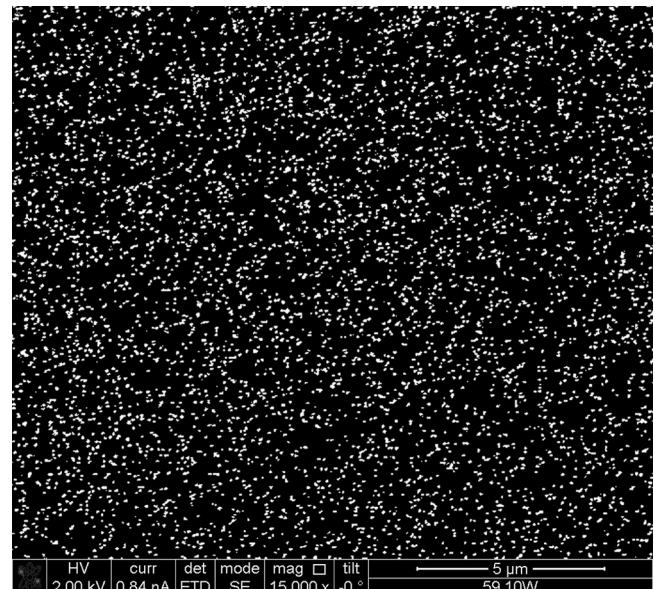
Figure 11. Top-view SEM image of sample IV: a grayscale threshold has been applied to convert the protruding head of the cone into white and the rest into black. The surface coverage of the crystalline cones is 21 cones per μm^2: with an average diameter of the protruding cone at the surface of 50 nm, this amounts to 4.1% surface coverage at a layer thickness of 86 nm.

J. Phys. D: Appl. Phys. **50** (2017) 065305

K Landheer *et al*
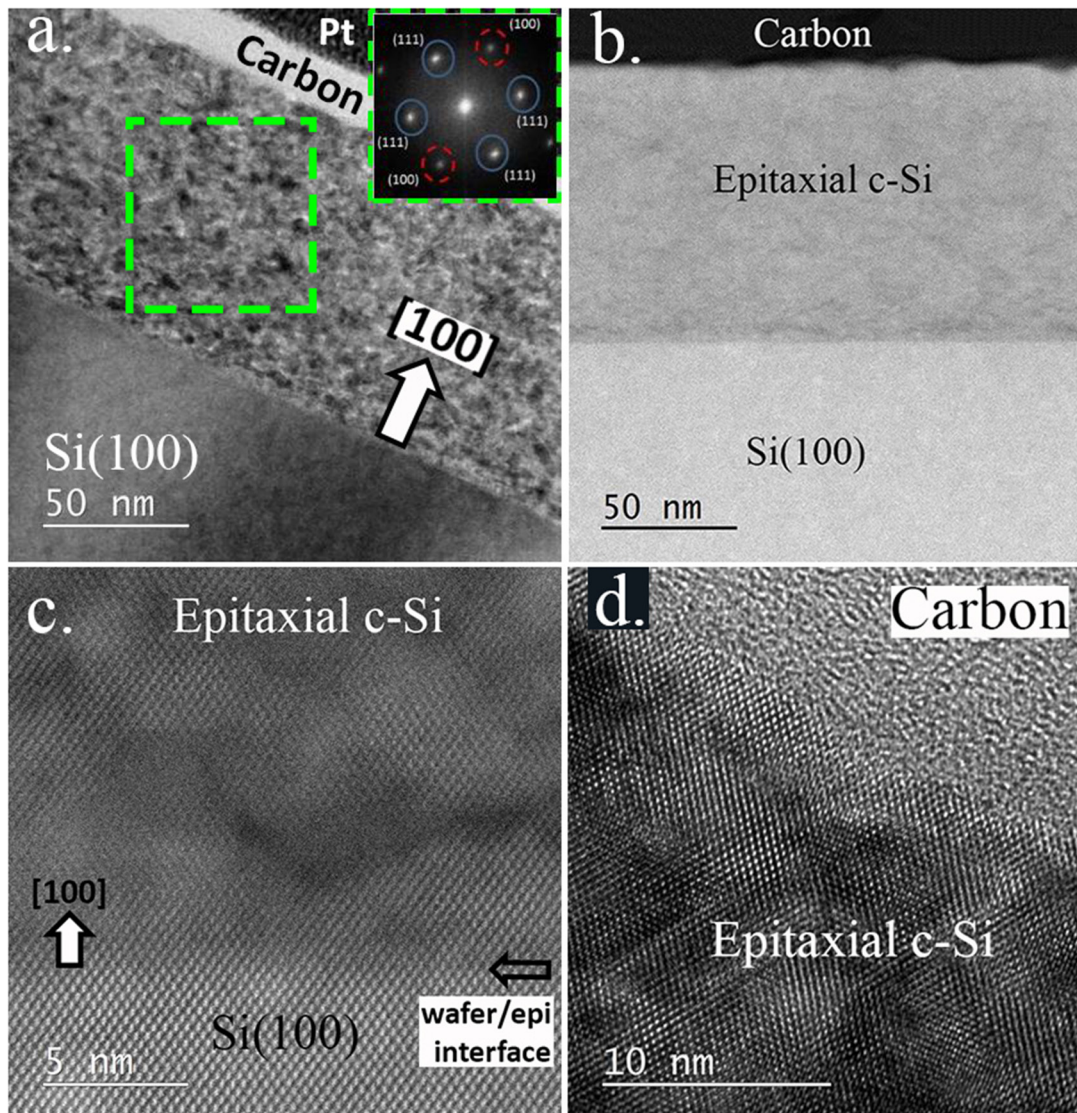
Figure 12. Sample V: epitaxial silicon layer of about 95 nm on HF-cleaned Si (1 0 0) wafer. (a) TEM cross-section imaged along the ⟨1 1 0⟩ zone axis. The epitaxial layer is single-crystalline: illustrated by the FFT of the dashed squared region. (b) HAADF-STEM image: darks spots in the epitaxial layer indicate the presence of voids. (c) HAADF-HR-STEM image: a perfect lattice continuation can be discerned (see horizontal arrow) at the epi/wafer interface. About 3–5 nm above the wafer surface, voids are observed (the darker regions in the STEM image). (d) HR-TEM image of the top of the epitaxial and the interface with the carbon protection layer. The epitaxial layer shows only a few monolayers of roughness.

Thus, the nucleation only takes place at the surface. The seeded growth may be initiated at small irregularities in the Si (1 1 1) substrate plane, such as kinks and steps. No rows of cones are observed in figure 11 and, therefore, step edges are excluded. It is unique that no cones are seeded inside the a-Si:H layer, which is normally observed for mixed-phase μc-Si:H growth.

The results showed that the crystallinity of the Si deposited strongly depends on the state of the substrate surface. Epitaxial Si growth is observed on the Si (1 0 0) substrate of samples II and V, that were co-deposited with samples I and IV, respectively. The hydrogen content of these epitaxial layers is low ($c_H < 5.8$ %) and similar to the c_H of μc-Si:H grown close to the a-Si:H to μc-Si:H transition [31]. The

microstructure parameter of our epitaxial samples is high ($R^{*\prime}$ is about 0.75) and this can be correlated to the large presence of voids: sample II and V have a void content of 3.5% and 5.5%, respectively. It should be noted that the epitaxial growth of sample V is nearly continuous in the ⟨1 0 0⟩ direction, until the top of the 95 nm thick layer. In the case of equilibrated growth, the slowest growth is in the ⟨1 1 1⟩ direction [37]. The deposition rates of samples II and V are 0.172 and 0.181 nm s^{-1}, respectively. Both the fast growth and chemical sputtering by H_y^+ ions can introduce voids in the epitaxial Si layer. It is most likely caused by fast growth, since no voids were discerned in the crystalline cones of sample IV.

J. Phys. D: Appl. Phys. **50** (2017) 065305

K Landheer *et al*

5. Conclusions

In this study, we investigated the passivation quality of i-a-Si:H layers near and in the a-Si:H to epitaxial Si transition regime by varying the silane fraction S_F and discharge power density P_{rf} of the SiH_4–H_2 VHF PECVD discharge. Excellent passivation samples on Si (1 1 1) wafers ($\tau_{eff} = 7.2$ ms upon annealing for a 24 nm i-a-Si:H layer) were obtained with depositions at low silane concentration ($S_F = 1.7\%$) and low substrate temperature ($T_{subs} = 130$ °C). This i-a-Si:H material was also used in a flat SHJ solar cell and resulted in a solar cell efficiency of 17.2%.

A slight increase of the deposition discharge power produced an a-Si:H layer with sparsely embedded crystalline cones. HR-TEM observations showed that the growth parameters used are on the edge of the crystallization regime: a high density of stacking faults (twin boundaries) in the epitaxial cones, and the inclusion of a high void density in the epitaxial layer co-deposited on Si (1 0 0). The effective carrier lifetime of the passivation sample with local epitaxy was poor and did not improve upon post-deposition annealing. A sparse surface coverage of cones seeded on the Si (1 1 1) substrate is most probably enabled by a combination of nucleation at steps and kinks in the {1 1 1} surface and intense ion bombardment at low silane concentration. Thus, we conclude that sparse local epitaxial growth on Si (1 1 1) is enough to obstruct crystalline silicon surface passivation by amorphous silicon.

References

[1] Adachi D, Hernández J L and Yamamoto K 2015 *Appl. Phys. Lett.* **107** 233506
[2] Shu Z, Das U, Allen J, Birkmire R and Hegedus S 2015 *Prog. Photovolt., Res. Appl.* **23** 78–93
[3] Fujiwara H and Kondo M 2007 *Appl. Phys. Lett.* **90** 13503
[4] Leendertz C, Mingirulli N, Schulze T F, Kleider J P, Rech B and Korte L 2011 *Appl. Phys. Lett.* **98** 202108
[5] De Wolf S and Kondo M 2007 *Appl. Phys. Lett.* **90** 42111
[6] Mews M, Schulze T F, Mingirulli N and Korte L 2013 *Appl. Phys. Lett.* **102** 122106
[7] Meddeb H, Bearda T, Dimassi W, Abdulraheem Y, Ezzaouia H, Gordon I, Szlufcik J and Poortmans J 2015 *Phys. Status Solidi* **9** 53–6
[8] Descoeudres A *et al* 2011 *Appl. Phys. Lett.* **99** 123506
[9] De Wolf S, Olibet S and Ballif C 2008 *Appl. Phys. Lett.* **93** 32101
[10] Street R, Kakalios J, Tsai C and Hayes T 1987 *Phys. Rev.* B **35** 1316–33
[11] Langford A A, Fleet M L, Nelson B P, Lanford W A and Maley N 1992 *Phys. Rev.* B **45** 13367–77
[12] Schüttauf J W A, van der Werf C H M, Kielen I M, van Sark W G J H M, Rath J K and Schropp R E I 2012 *J. Non-Cryst. Solids* **358** 2245–8
[13] Descoeudres A, Barraud L, Bartlome R, Choong G, De Wolf S, Zicarelli F and Ballif C 2010 *Appl. Phys. Lett.* **97** 183505
[14] De Wolf S, Ballif C and Kondo M 2012 *Phys. Rev.* B **85** 113302
[15] Tanaka M, Taguchi M, Matsuyama T, Sawada T, Tsuda S, Nakano S, Hanafusa H and Kuwano Y 1992 *Japan. J. Appl. Phys.* **31** 3518–22
[16] Demaurex B, Bartlome R, Seif J P, Geissbühler J, Alexander D T L, Jeangros Q, Ballif C and De Wolf S 2014 *J. Appl. Phys.* **116** 53519
[17] Das U K, Burrows M Z, Lu M, Bowden S and Birkmire R W 2008 *Appl. Phys. Lett.* **92** 63504
[18] Olibet S, Monachon C, Hessler-Wyser A, Vallat-Sauvain E, Wolf S D, Fesquet L, Damon-Lacoste J and Ballif C 2008 *Proc. 23rd European Photovoltaic Solar Energy Conf.* pp 1140–4
[19] Collins R W, Ferlauto A S, Ferreira G M, Chen C, Koh J, Koval R J, Lee Y, Pearce J M and Wronski C R 2003 *Sol. Energy Mater. Sol. Cells* **78** 143–80
[20] Fujiwara H, Kaneko T and Kondo M 2007 *Appl. Phys. Lett.* **91** 133508
[21] Hricovini K *et al* 1993 *Phys. Rev. Lett.* **70** 1992–5
[22] Landheer K, Goedheer W J, Poulios I, Schropp R E I and Rath J K 2016 *J. Appl. Phys.* **120** 053304
[23] Landheer K, Goedheer W J, Poulios I, Schropp R E I and Rath J K 2016 *Phys. Status Solidi* a **213** 1680
[24] Sinton R A and Cuevas A 1996 *Appl. Phys. Lett.* **69** 2510
[25] Jellison G E and Modine F A 1996 *Appl. Phys. Lett.* **69** 371
[26] Cardona M 1983 *Phys. Status Solidi* b **118** 463–81
[27] Schulze T F, Beushausen H N, Leendertz C, Dobrich A, Rech B and Korte L *Appl. Phys. Lett.* **96** 252102
[28] Rath J K, Schropp R E I and Cabarrocas P R I 2008 *Phys. Status Solidi* c **5** 1346–9
[29] Kondo M, Fujiwara H and Matsuda A 2003 *Thin Solid Films* **430** 130–4
[30] Shi T S, Sahu S N, Oehrlein G S, Hiraki A and Corbett J W 1982 *Phys. Status Solidi* a **74** 329–41
[31] Kroll U, Meier J, Torres P, Pohl J and Shah A 1998 *J. Non-Cryst. Solids* **227–30** 68–72
[32] Palmans J, Kessels W M M and Creatore M 2014 *J. Phys. Appl. Phys.* **47** 224003
[33] Otobe M, Kimura M and Oda S 1994 *Japan. J. Appl. Phys.* **33** 4442–5
[34] Ma Z Q, Zheng Y F and Liu B X 1998 *Phys. Status Solidi* a **169** 239–48
[35] Street R A 1991 *Phys. Rev.* B **43** 2454–7
[36] Hamers E A G, Fontcuberta i Morral A, Niikura C, Brenot R and Roca i Cabarrocas P 2000 *J. Appl. Phys.* **88** 3674
[37] Drosd R 1982 *J. Appl. Phys.* **53** 397